

Rapid Water Permeation Through Carbon Nanomembranes with Sub-Nanometer Channels

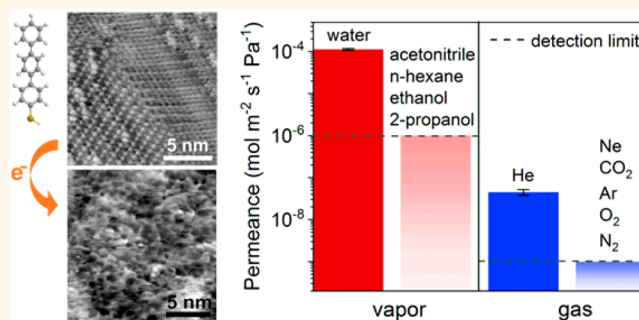
Yang Yang,[†] Petr Dementyev,[†] Niklas Biere,[‡] Daniel Emmrich,[†] Patrick Stohmann,[†] Riko Korzetz,[†] Xianghui Zhang,[†] André Beyer,[†] Sascha Koch,[†] Dario Anselmetti,[‡] and Armin Götzhäuser^{*,†}

[†]Physics of Supramolecular Systems and Surfaces, Faculty of Physics and [‡]Experimental Biophysics and Applied Nanoscience, Faculty of Physics, Bielefeld University, 33615 Bielefeld, Germany

S Supporting Information

ABSTRACT: The provision of clean water is a global challenge, and membrane filtration is a key technology to address it. Conventional filtration membranes are constrained by a trade-off between permeance and selectivity. Recently, some nanostructured membranes demonstrated the ability to overcome this limitation by utilizing well-defined carbon nanoconduits that allow a coordinated passage of water molecules. The fabrication of these materials is still very challenging, but their performance inspires research toward nanofabricated membranes. This study reports on molecularly thin membranes with sub-nanometer channels that combine high water selectivity with an exceptionally high permeance. Carbon nanomembranes (CNMs) of ~ 1.2 nm thickness are fabricated from terphenylthiol (TPT) monolayers. Scanning probe microscopy and transport measurements reveal that TPT CNMs consist of a dense network of sub-nanometer channels that efficiently block the passage of most gases and liquids. However, water passes through with an extremely high permeance of $\sim 1.1 \times 10^{-4} \text{ mol} \cdot \text{m}^{-2} \cdot \text{s}^{-1} \cdot \text{Pa}^{-1}$, as does helium, but with a ~ 2500 times lower flux. Assuming all channels in a TPT CNM are active in mass transport, we find a single-channel permeation of ~ 66 water molecules $\cdot \text{s}^{-1} \cdot \text{Pa}^{-1}$. This suggests that water molecules translocate fast and cooperatively through the sub-nanometer channels, similar to carbon nanotubes and membrane proteins (aquaporins). CNMs are thus scalable two-dimensional sieves that can be utilized toward energy-efficient water purification.

KEYWORDS: membrane separation, 2D material, water purification, sub-nanometer channels, self-assembled monolayer



The development of energy-efficient water treatment technology is a global challenge and spans a wide range of applications from membrane distillation to seawater desalination. In standard purification devices, untreated water is pressed through membranes that separate its constituents in a solution-diffusion process, which is characterized by a trade-off between selectivity and flow-rate.^{1,2} The need for high pressure further leads to high energy consumption and requires high mechanical stability.³ To overcome these constraints, nanotechnology came up with carbon membranes that separate liquids by nanoscale confinement.^{4–6} Although these nanoconduit devices are still in their infancy and a mass fabrication seems remote, the emerging field of carbon nanofluidics⁷ already provides fascinating insights on materials separation. An example is the directed water transport through biological membranes in living cells, achieved by aquaporin (water pore) proteins with a channel diameter of only ~ 0.3 nm, just wide enough for one molecule.⁸ Aquaporin proteins have also been

embedded in artificial membranes and used as water filters.⁹ Another example are carbon nanotubes (CNTs), through which the molecular transport was studied theoretically^{10,11} and experimentally.^{12–14} Like biological channels, CNTs show extraordinary high water flow-rates owing to their smooth interfaces and single-file motions.^{10–13} Two-dimensional (2D) carbon, that is, graphene, is impermeable for water. However, graphene sheets have been perforated by ion bombardment with nanometer-size holes producing a molecular sieve that permits water/ion separation with high selectivity and flow-rate.^{15–17} Graphene oxide (GO) also shows low-friction water flow through the confined 2D space between stacked GO sheets.⁵ GO stacks are easily fabricated, but GO membranes swell in water leading to a reduced selectivity.¹⁸ The above

Received: February 16, 2018

Accepted: May 3, 2018

Published: May 9, 2018

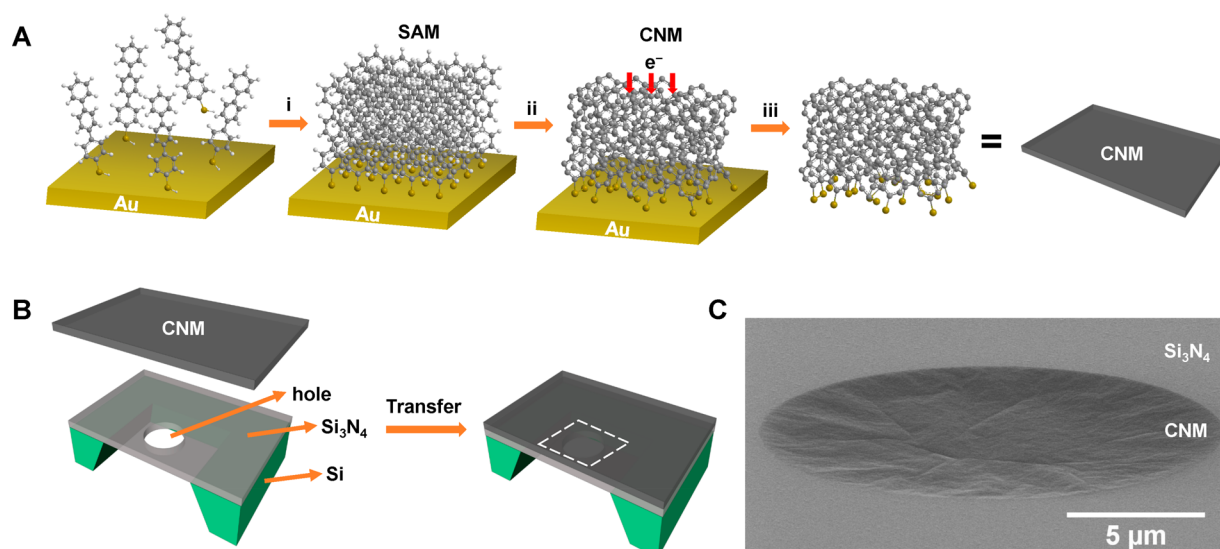


Figure 1. Fabrication and transfer of TPT CNMs. (A) Fabrication of CNMs from TPT precursors: (i) TPT molecules self-assemble on a gold substrate; (ii) exposure of the monolayer to electrons forms intermolecular cross-links, and SAMs are converted into CNMs; and (iii) the CNM detaches from the Au substrate. (B) Schematic of transferring the CNM onto a Si₃N₄/Si chip device with a single microhole of 18 μm. The area marked with white dashed lines indicates the imaging area shown in (C). (C) HIM image (secondary-electron signal) of a freestanding CNM suspended over the microhole. The sample was tilted by ~75° for imaging.

nanomaterials efficiently filter water by physical confinement, nevertheless, a simple approach to fabricate a scalable 2D membrane with a high density of sub-nanometer (sub-nm) pores that combines high water permeance with high selectivity has not yet been developed.

Carbon nanomembranes (CNMs) are mechanically stable nanosheets that are simply made by irradiation-induced cross-linking of surface bound self-assembled monolayers (SAMs).¹⁹ In this article, we show that a ~1.2 nm thin CNM made from terphenylthiol (TPT) molecules consists of a dense network of sub-nm channels and exhibits an exceptionally high water permeance and high selectivity. The fabrication of the TPT CNM is schematically shown in Figure 1A. It utilizes a sequence of monolayer assembly (i), electron radiation-induced cross-linking (ii), and a lift-off of the 2D network of cross-linked molecules (iii). The result is a membrane with the thickness of one TPT molecule, whose properties are controlled by the fabrication process.²⁰ Figure 1C shows a helium ion micrograph of a freestanding TPT CNM that suspends over an 18 μm-circular hole in a Si₃N₄ support forming a tight seal, which itself rests on a silicon frame chip device. The architecture and composition of TPT CNMs were investigated by scanning tunneling microscopy (STM), atomic force microscopy (AFM), helium ion microscopy (HIM), and X-ray photoelectron spectroscopy (XPS). The molecular transport properties were studied by mass-loss methods and permeation measurements in vacuum. The transport mechanism of water molecules through CNMs will also be discussed.

RESULTS AND DISCUSSION

Characterization of TPT CNMs. To explore the structure and morphology of TPT SAMs and CNMs, STM and AFM were employed. The topography image of a TPT SAM showed that TPT molecules adsorb in different but highly oriented and densely packed monolayer domains on Au(111) surface^{21–23} (Figure 2A and Figure S1). The molecular corrugations of 0.58 ± 0.01 nm and 1.03 ± 0.02 nm extracted from line profiles in Figure 2C are in accordance with other reported values.^{22,23}

XPS measurements revealed that the TPT molecules were arranged in a densely packed monolayer of ~1.2 nm thickness, as determined from the attenuation of the Au 4f7/2 photoelectrons.^{24,25} After electron irradiation, the monolayer structure is completely reorganized. Tapping mode AFM images show that the resulting CNM contains a dense network of channels (Figure 2B–E and Figures S2–4). From these, average channel diameters of ~0.7 nm (see [Estimation of Pore Diameters from AFM section and Figure S3](#)) and an areal density of ~10¹⁸ m⁻² were estimated (Figure S4). Earlier spectroscopic and quantum chemical studies^{19,25,26} provided evidence that the electron irradiation of aromatic SAMs mainly results in the loss of the hydrogen content due to the C–H bond cleavage, while the carbon content was conserved,²⁶ which agrees with our XPS results (Figure S5). The sulfur spectrum of TPT SAM shows a single species with a S 2p_{3/2} binding energy of 162.0 eV that is attributed to thiolates on gold (R–S–Au).²⁵ After irradiation, a new sulfur species is observed which is assigned to organosulfides,²⁷ suggesting that some sulfur groups no longer bond to gold but form sulfides (R–S–R) or disulfides (R–S–S–R) by linking adjacent molecules.^{25,27} The occurrence of these cross-linking reactions could induce the formation of sub-nm conduits within the CNMs. From the above, we conclude that the channels in CNMs develop in the irradiation process after C–H and RS–Au bonds are cleaved and new C–C bonds are formed.

Selective Water Permeation. Molecular transport through TPT CNMs was then investigated with two different permeation experiments. First, water permeation through CNMs was studied by a mass-loss method (Figure 3A).²⁸ A CNM-covered silicon frame was glued onto a stainless-steel container partially filled with 400 μL of Milli-Q water. The container was placed into a low-humidity environment, and the water flux through the CNM was determined by a high-precision microbalance. As a reference, we first measured the water flow rate through an 18 μm-sized hole without CNMs, observing a mass loss rate of 48.1 μg/h (Figure 3B). When the hole was covered with CNMs, the mass loss was 6.6 μg/h,

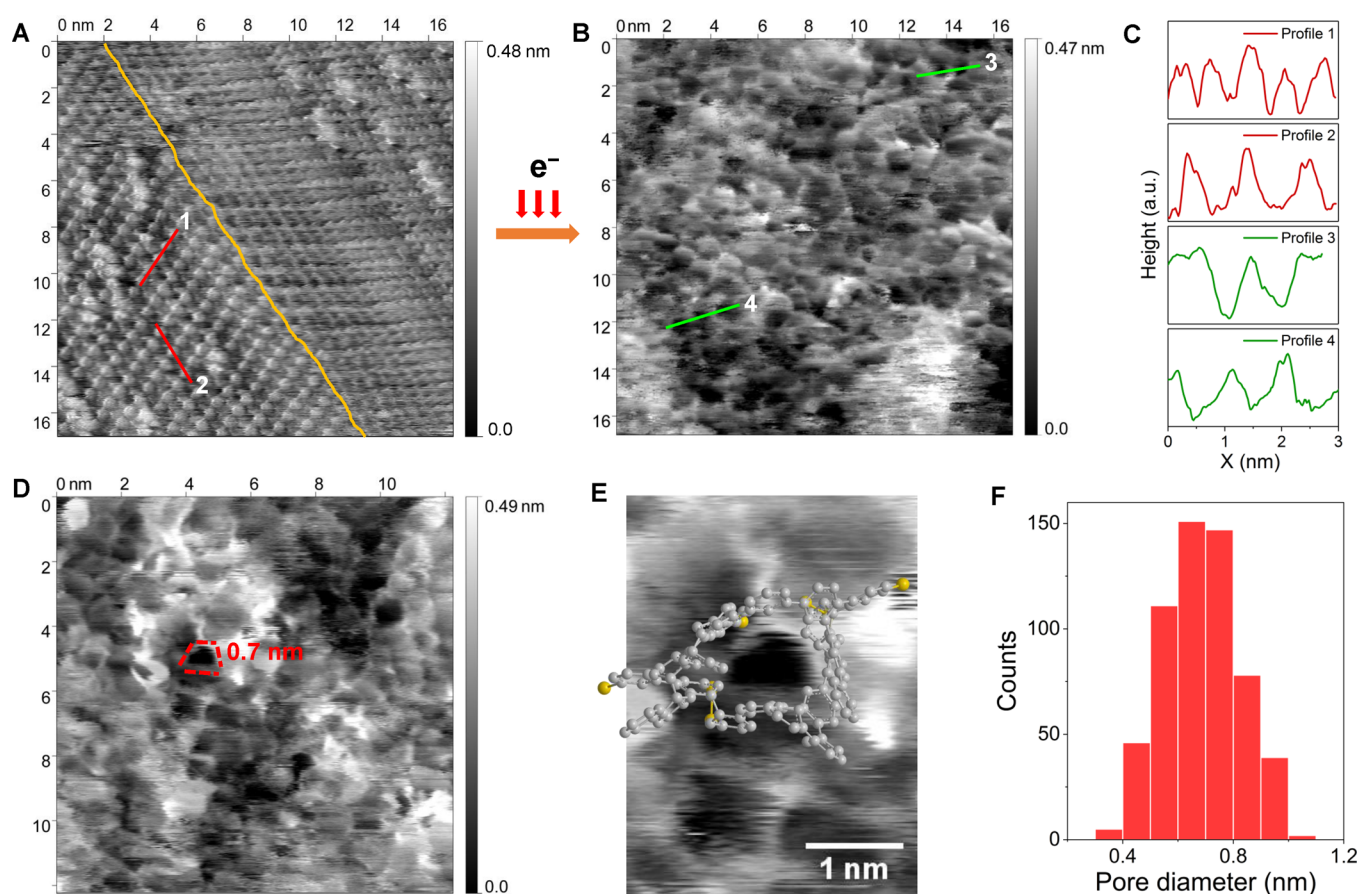


Figure 2. Morphology of TPT SAM and CNM. (A) STM image of TPT SAM measured at room temperature in ultrahigh vacuum (UHV) ($U_{\text{Bias}} = 790$ mV, $I_{\text{T}} = 40$ pA). A domain boundary between two domains is marked by a yellow line. (B) AFM image of TPT CNM measured at 93 K in UHV *via* AFM tapping mode of operation (amplitude set point $A = 8.9$ nm, center frequency $f_0 = 274.9$ kHz). (C) Extracted line profiles in (A) (marked with red lines) and (B) (marked with green lines). (D) AFM image of TPT CNM measured at 93 K in UHV *via* AFM tapping mode of operation (amplitude set point $A = 7.6$ nm, center frequency $f_0 = 274.8$ kHz). (E) A drawing of the marked pore in (D) by laterally cross-linking seven TPT molecules using the Chemdraw program (PerkinElmer Informatics). (F) The estimated pore diameter distributions (0.7 ± 0.1 nm, the error bar denotes standard deviation) extracted from the acquired AFM images. All the STM and AFM images shown were drift corrected.

which corresponds to a permeance of 1.1×10^{-4} mol·m⁻²·s⁻¹·Pa⁻¹. This value is comparable to the permeances of other reported nanomaterials (aquaporin biomimetic membranes,²⁹ graphene-based membranes,^{5,15} and CNT-parylene composite films¹⁴) measured by similar methods and 2–3 orders of magnitude higher than that of commercial breathable polymer membranes.³⁰ With the same method, other (polar and nonpolar) liquids like acetonitrile, *n*-hexane, ethanol, and 2-propanol were also tested, and no mass loss was detected, indicating that CNMs act as molecular sieves, which only allow the passing of molecules below a certain size. In addition, mass loss experiments with containers upside down resulted in the same permeance as with containers in the upright position, which suggests that the observed fast water transport is likely attributed to a liquid water film on the CNM (Figure 3C).

The high water permeance of CNMs was independently confirmed by vapor transport measurements in vacuum (Figure 3D). One side of the CNMs was exposed to water vapor under controlled relative humidity (RH), and the flow of permeating molecules was detected by a mass spectrometer placed behind the CNMs. As a reference, we employed a nanoaperture produced in a 100 nm-thick Si₃N₄ membrane (Figure S7). A linear response of the spectrometer to the amount of gas in the permeation cell is observed over the range of interest. Figure 3E

illustrates the principle of the gas permeation measurements (see Methods). After the permeation experiments, all CNMs have been examined by helium ion microscopy to ascertain that they were not damaged during the transport measurements (Figure S8). Within the experimental accuracy, the water permeance at saturation conditions (100% RH) agrees well with the gravimetric results (Figure 3F). At lower humidity, the permeance dropped. As at high humidity, more water vapor adsorbed on solid surfaces,³¹ the higher permeance at saturation pressure is most likely to be attributed to more water adsorption. Unlike GO membranes,⁵ the permeance of CNMs did not vanish with decreasing humidity but remained at $\sim 2.0 \times 10^{-5}$ mol·m⁻²·s⁻¹·Pa⁻¹ at RH below 20%. This seems related to a transition between different transport mechanisms. Interestingly, the permeance of helium ($\sim 4.5 \times 10^{-8}$ mol·m⁻²·s⁻¹·Pa⁻¹) is 2500 times lower than that of water, although they have similar kinetic diameters³² (0.265 nm for water and 0.26 nm for helium). No noticeable permeation was detected for other gas molecules with kinetic diameters larger than 0.275 nm (Ne, CO₂, Ar, O₂, N₂). This is consistent with the picture that the CNM is a “sieve” composed of a network of sub-nm channels. However, looking at the kinetic diameters of the nonpermeating molecules, the AFM-based estimation of ~ 0.7 nm for the average channel diameter appears to be too large.

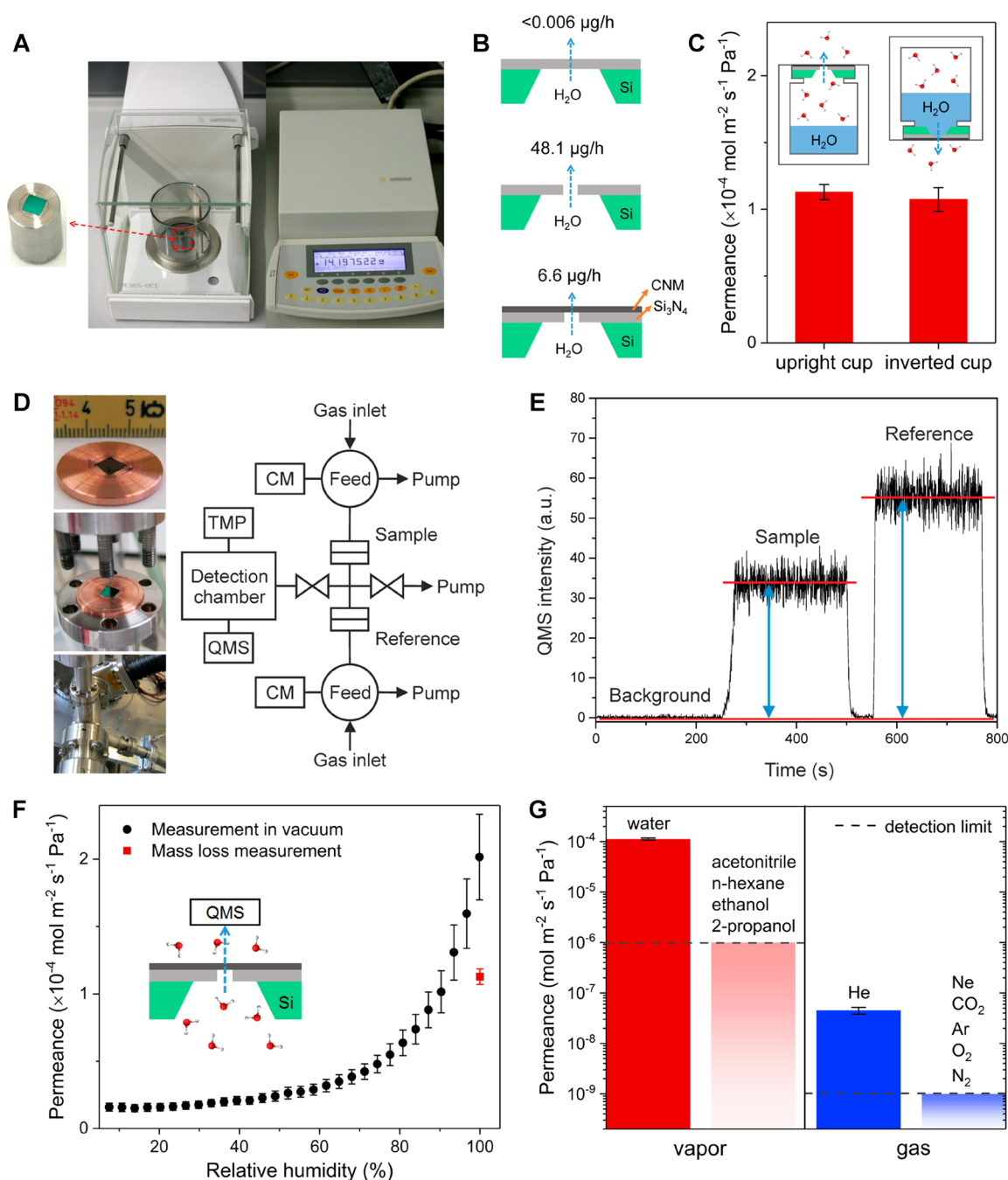


Figure 3. Molecular transport through TPT CNMs. (A) Photograph of the experimental setup of mass-loss methods. (B) Mass-loss rates measured in upright position for $\text{Si}_3\text{N}_4/\text{Si}$ chip (top), an $18\ \mu\text{m}$ -sized hole without (middle), and covered with CNMs (bottom). (C) Water permeance of TPT CNMs measured by mass loss—upright cup (liquid water not in contact with CNMs) and inverted cup (liquid water in contact with CNMs). (D) Schematic and photographs of the gas permeation setup. The permeance was detected by a quadrupole mass spectrometer (QMS). (E) Exemplary mass spectrometry analysis: The signal intensity of instrumental background noise, a CNM sample, and the reference. (F) Water permeance of TPT CNMs as a function of the RH in the feed chamber measured in the vacuum apparatus. The red square is the value measured by the mass loss methods (upright cup). (G) Permeances of vapors and gases of TPT CNMs measured by two different experiments (see A, D). The dashed lines indicate the respective detection limits of our measurements. The detection limit of vapor permeation measurements is related to the sensitivity of the balance and the duration of the experiment. The detection limit of gas permeation measurements depends on the instrumental background noise (a signal produced with a blank test) of the mass spectrometer. The error bars denote standard error of mean within 4–6 samples.

This is possibly because the AFM images were obtained from a tapping mode operation which are governed by short-range repulsive interaction forces,³³ whereas the permeation through $\sim 1.2\ \text{nm}$ long channels in TPT CNMs may also be affected by (attractive) long-range forces. In addition, the channels may

possess inner structures inaccessible by AFM imaging. Assuming that channels are narrower in the middle and wider at their ends, this would reduce the active pore size in permeation. This view is further supported by an estimation of pore sizes from classical flow models (see [Supporting](#)

Information “Estimation of pore diameters from classical flow models”). Hence, the ~ 0.7 nm diameter determined from AFM images must be considered as an upper limit for the active pore diameters.

Understanding the Permeation Behavior. To understand the distinct differences between water and helium, the molecular transport through this sub-nm channel is discussed. The permeation process basically involves three steps: (i) adsorption on the surface and diffusion to the channel, (ii) transport across the channel, and (iii) dissociation from the channel and desorption from the surface. For the first step, we compare water and helium by calculating their molar densities.³⁶ The density of liquid water is $5.6 \times 10^4 \text{ mol}\cdot\text{m}^{-3}$, while the density of helium is only $5.3 \text{ mol}\cdot\text{m}^{-3}$ at a pressure of 130 mbar. Thus, the probability that a water molecule in a water film reaches the channel is much higher than that of a helium atom in the gas phase. Assuming that all sub-nm channels in CNMs are active in mass transport, a single-channel permeation coefficient Π can be calculated: $\Pi = P \times N_A / \sigma$, where P is the permeance ($\text{mol}\cdot\text{m}^{-2}\cdot\text{s}^{-1}\cdot\text{Pa}^{-1}$), N_A is the Avogadro number (mol^{-1}), and σ is the areal pore density (m^{-2}). The obtained value of ~ 66 water molecules $\cdot\text{s}^{-1}\cdot\text{Pa}^{-1}$ compares well with the values obtained for carbon nanotubes and aquaporin proteins^{11,34,35} (Figure 4). It is known that water

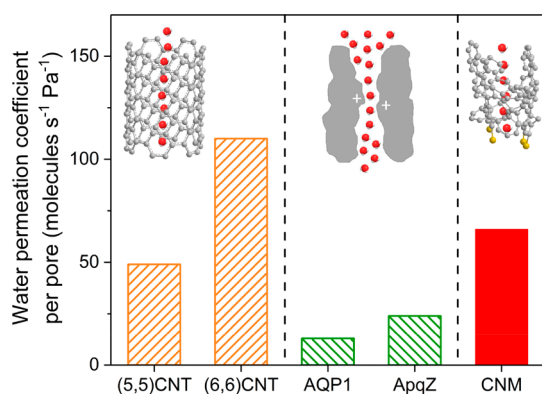


Figure 4. A comparison of single-channel water permeation coefficients between different membranes. Molecular dynamics simulation was used to study the permeation coefficients of CNTs ((5,5)CNT,¹¹ (6,6)CNT¹¹), and a stopped-flow apparatus was employed to characterize aquaporins (AQP1,³⁴ AqpZ³⁵). The permeation coefficient of TPT CNM was calculated from dividing the measured permeance by the areal density of nanochannels estimated from the AFM images.

molecules confined in sub-nm channels form water chains attributed to the strong and short time hydrogen-bonding character between neighboring molecules,³⁷ which allows water to rapidly rush through as a single file. This cooperative effect is also well supported by the permeation data shown in Figure 3C. Since helium exhibits no directed and comparatively strong interactions at room temperature, a concerted and cooperative transport is lacking. Hence, water passes through the channel apparently faster than helium in the second step (see also Figure S9). In addition to the aforementioned, it is also possible that the CNM pores are not rigid, and the motion of the hydrogen-bonded water molecules inside the channel enlarges the pores and allows the preferential permeation of water. This structural feature of pores will be explored in future studies with liquid mixtures, such as water/ion separation.

CONCLUSION

In summary, we found that TPT CNMs are perforated by a high density of sub-nm channels that filter water with very high permeance and high molecular selectivity. The water permeance determined from the mass-loss method is in good agreement with the permeance detected by mass spectrometry. A rapid water permeation is observed that is most likely attributed to a coordinated water transport within the sub-nanometer channels, similar to the mechanisms responsible for the rapid water flow through aquaporin and carbon nanotubes. Unlike other carbon materials, CNMs are built in a versatile and scalable fabrication process, allowing membranes to be customized with nanometer thickness and chemistry.^{19,20} The possibility to modify CNMs by different functional groups¹⁹ at the surface will allow further pathways to tailor and optimize the selectivity of the translocation process in future applications. These advantages make CNMs a highly promising material for efficient separations, such as dehydration of organics, dehumidification of gases, and purification of water.

METHODS

Fabrication of Freestanding TPT CNMs. The preparation of TPT SAM is described elsewhere.²⁰ Conversion of SAMs into CNMs was achieved by using an electron flood-gun in a high vacuum ($< 3 \times 10^{-7}$ mbar) and employing 100 eV electrons and a dose of 50 mC/cm². The target substrate used for permeation measurements was a Si₃N₄/Si chip which consists of a 500 nm-thick silicon nitride membrane on top of a 200 μm -thick silicon supporting frame, and a circular hole with diameter 5–50 μm was made in the silicon nitride membrane (Silson Ltd., UK). CNMs were transferred onto Si₃N₄/Si chips with the assistance of PMMA coatings.³⁸

Characterization and Microscopy Imaging. X-ray photoelectron spectroscopy (XPS) was employed to characterize the chemical changes occurring after irradiation by using an Omicron Multiprobe system with a base pressure of $\sim 10^{-10}$ mbar. The system consists of a monochromatic X-ray source (Al K α) and a hemispherical electron analyzer (SPHERA). The XPS were measured at a photoelectron emission angle of $\sim 13^\circ$. The spectra were processed using the CasaXPS program. The HIM images were acquired in secondary electron or bright-field ion transmission mode with a Zeiss ORION Plus helium ion microscope. The microscope was operated at a beam energy of 35 keV and an ion beam current of 1 pA. Charges on the sample were neutralized by using a build-in electron floodgun for avoiding charge-induced ruptures. The STM image of TPT SAM was obtained by using a multichamber UHV system (Omicron) with a base pressure of 5×10^{-11} mbar. The measurement was operated at room temperature. The tunneling tip was prepared by electrochemical etching (3 mol $\cdot\text{L}^{-1}$ NaOH solution) of a tungsten wire and further processed *in situ* by sputtering with Ar⁺ ions ($p_{\text{Ar}} = 3 \times 10^{-10}$ mbar, $E = 1$ keV, $t = 1$ –2 min). The AFM images of TPT SAM and CNM were acquired using a RHK UHV 7500 system (5×10^{-11} mbar) with R9 controller. The measurements of TPT SAM and TPT CNM were conducted in the noncontact operation mode and the amplitude-modulated tapping operation mode, respectively, at room temperature and 93 K using a liquid nitrogen flow cryostat. Before measurements, the TPT SAM samples were first annealed in UHV for 1 h at 323 K and later on 1 h at 333 K for removal of residual adsorbates; the TPT CNM samples were annealed in UHV at 348 K for 30 min. The AFM tips were sputtered with Ar⁺ ions at 680 eV for 90 s. For the AFM images, Tap300Al-G force sensors ($\sim 40 \text{ N}\cdot\text{m}^{-1}$, $\sim 280 \text{ kHz}$, $Q \sim 10000$, Budget Sensors) were used. Analysis and post-processing (including corrections for thermal drift and polynomial background subtraction) of the STM and AFM data occurred in the open-source software package Gwyddion (<http://gwyddion.net/>).³⁹

Estimation of Pore Diameters from AFM. Pore diameters d_{pore} were estimated manually by measuring the area of the pores (A_{pore}) shown in AFM images using the mask drawing tool in Gwyddion (see

Figure S3 for example pores). The pore diameter was calculated by assuming that all pores are circular.

$$d_{\text{pore}} = \sqrt{\frac{4A_{\text{pore}}}{\pi}} \quad (1)$$

Mass-Loss Measurements. Water permeation through CNMs was studied with mass loss measurements (Figure 3).²⁸ Si₃N₄/Si chips with 18 μm-sized holes were used to prepare freestanding CNMs. The CNM-covered Si chips were glued by epoxy on top of a container which was filled with 400 μL of Milli-Q water. The experiments will start around 15 h later to make sure that the RH inside the container reaches 100% and a steady state of the mass change is reached. To confirm the reliability of the setup, a control measurement was first done with different-sized open apertures (Figure S6). The container was placed into an enclosed oven with a constant temperature (30 ± 0.1 °C), and the RH inside the oven was controlled around 15% ± 2% by saturated LiCl solution.⁴⁰ Due to differential water vapor pressure inside and outside the container, water will evaporate in the container and then permeate through the CNM. The mass loss of the container was measured after a week by using a microbalance (Sartorius ME36S with a sensitivity of 1 μg). The water permeance of the CNMs can be calculated by the following equations:

$$P = \frac{\Delta m/M}{A \times t \times \Delta p} \quad (2)$$

where Δm is the mass change of the container (g), M is molecular mass (g·mol⁻¹), A is the membrane area (m²), t is time interval for an experiment (s), Δp is vapor pressure difference (Pa). In this study, Δp is around 3600 Pa.

Gas Permeation. In order to characterize gas permeation through free-standing CNMs, we adopted an approach used for ultrathin polymeric membranes.⁴¹ The scheme of the experiment is shown in Figure 3D. A suspended CNM sample was glued onto a 2 mm-thick copper disk compatible with a CF flange. The assembled sample was further mounted in a homemade permeation cell representing a multiport CF vessel. The cell was designed to have two ports for membrane and reference samples providing identical pathways for incoming molecules. The permeation cell was connected to a high-vacuum chamber equipped with a quadrupole mass spectrometer (Hal-1001 Hiden Analytical) and with a base pressure of $\sim 2 \times 10^{-9}$ mbar. The upstream side of the sample was exposed to variable amounts of anhydrous gases or water vapors as controlled by a capacitance manometer (MKS Baratron Type 626). The membrane permeance was quantified by the mass spectrometer with a help of a reference sample which can be separately fed by a gas of interest. To ensure the mass spectrometer was not overwhelmed by large quantities of water vapor, Si₃N₄/Si chips with 5 μm-sized holes were used for preparing freestanding CNMs measured in vacuum system. To start a gas permeation measurement, we record the mass spectrometer background signal corresponding to residual concentration of the species of interest in the detection chamber, then we feed the CNM sample with the gas of interest and measure the signal of the permeating molecules. When the chamber is evacuated and the background signal is recovered, we supply the gas of interest to a reference sample and detect the respective signal. The experimental data were evaluated as following:

$$P = \frac{p_{\text{ref}} \times I_{\text{sample}} \times A_{\text{ref}}}{p_{\text{sample}} \times I_{\text{ref}} \times A_{\text{sample}}} \times \frac{1}{\sqrt{2\pi mkT} \times N_A} \quad (3)$$

where p_{sample} and p_{ref} are feed pressures applied to the membrane and reference samples, respectively, I_{sample} and I_{ref} are mass spectrometer signals corresponding to the membrane and reference samples, A_{ref} is area of the reference aperture, A_{sample} is membrane area, m is molecular mass of the gas of interest, k is the Boltzmann constant, T is temperature, and N_A is the Avogadro constant. The experiments were performed at room temperature.

ASSOCIATED CONTENT

Supporting Information

The Supporting Information is available free of charge on the ACS Publications website at DOI: 10.1021/acsnano.8b01266.

Control measurements of mass-loss methods, estimation of pore diameters from classical flow models, additional AFM and STM images, estimation of pore density, XPS analysis, examination of membrane intactness with HIM, and supplementary discussion (PDF)

AUTHOR INFORMATION

Corresponding Author

*E-mail: ag@uni-bielefeld.de.

ORCID

Yang Yang: 0000-0003-4518-6411

Xianghui Zhang: 0000-0002-5544-5221

André Beyer: 0000-0002-9569-0344

Sascha Koch: 0000-0002-4155-3694

Dario Anselmetti: 0000-0002-8720-4369

Armin Gölzhäuser: 0000-0002-0838-9028

Notes

The authors declare the following competing financial interest(s): A.G. is a co-founder and shareholder of CNM Technologies GmbH, a company that specializes on the development of carbon nanomembranes. Y.Y., X.Z., and A.G. are co-authors of a patent for A Method for Separating Fluidic Water from Impure Fluids and a Filter, which is related to the published research.

ACKNOWLEDGMENTS

This work was supported by German Federal Ministry of Education and Research (BMBF) within the M-Era.net Program, project MOLFIL-CNM 03X0158A. N.B. and D.A. acknowledge funding from the Deutsche Forschungsgemeinschaft under the grant DA 370/8-1.

REFERENCES

- Werber, J. R.; Osuji, C. O.; Elimelech, M. Materials for Next-Generation Desalination and Water Purification Membranes. *Nat. Rev. Mater.* **2016**, *1*, 16018.
- Park, H. B.; Kamcev, J.; Robeson, L. M.; Elimelech, M.; Freeman, B. D. Maximizing the Right Stuff: The Trade-Off between Membrane Permeability and Selectivity. *Science* **2017**, *356*, eaab0530.
- Elimelech, M.; Phillip, W. A. The Future of Seawater and the Environment: Energy, Technology, and the Environment. *Science* **2011**, *333*, 712–718.
- Joshi, R. K.; Carbone, P.; Wang, F. C.; Kravets, V. G.; Su, Y.; Grigorieva, I. V.; Wu, H. A.; Geim, A. K.; Nair, R. R. Precise and Ultrafast Molecular Sieving through Graphene Oxide Membranes. *Science* **2014**, *343*, 752–754.
- Nair, R. R.; Wu, H. A.; Jayaram, P. N.; Grigorieva, I. V.; Geim, A. K. Unimpeded Permeation of Water through Helium-Leak-Tight Graphene-Based Membranes. *Science* **2012**, *335*, 442–444.
- Tunuguntla, R. H.; Henley, R. Y.; Yao, Y.-C.; Pham, T. A.; Wanunu, M.; Noy, A. Enhanced Water Permeability and Tunable Ion Selectivity in Subnanometer Carbon Nanotube Porins. *Science* **2017**, *357*, 792–796.
- Park, H. G.; Jung, Y. Carbon Nanofluidics of Rapid Water Transport for Energy Applications. *Chem. Soc. Rev.* **2014**, *43*, 565–576.
- Agre, P. Aquaporin Water Channels (Nobel Lecture). *Angew. Chem., Int. Ed.* **2004**, *43*, 4278–4290.

- (9) Tang, C.; Wang, Z.; Petrinic, I.; Fane, A. G.; Helix-Nielsen, C. Biomimetic Aquaporin Membranes Coming of Age. *Desalination* **2015**, *368*, 89–105.
- (10) Hummer, G.; Rasaiah, J. C.; Noworyta, J. P. Water Conduction through the Hydrophobic Channel of a Carbon Nanotube. *Nature* **2001**, *414*, 188–190.
- (11) Corry, B. Designing Carbon Nanotube Membranes for Efficient Water Desalination. *J. Phys. Chem. B* **2008**, *112*, 1427–1434.
- (12) Majumder, M.; Chopra, N.; Andrews, R.; Hinds, B. J. Nanoscale Hydrodynamics: Enhanced Flow in Carbon Nanotubes. *Nature* **2005**, *438*, 44.
- (13) Holt, J. K.; Park, H. G.; Wang, Y.; Stadermann, M.; Artyukhin, A. B.; Grigoropoulos, C. P.; Noy, A.; Bakajin, O. Fast Mass Transport through Sub-2-Nanometer Carbon Nanotubes. *Science* **2006**, *312*, 1034–1037.
- (14) Bui, N.; Meshot, E. R.; Kim, S.; Peña, J.; Gibson, P. W.; Wu, K. J.; Fornasiero, F. Ultrabreathable and Protective Membranes with Sub-5 nm Carbon Nanotube Pores. *Adv. Mater.* **2016**, *28*, 5871–5877.
- (15) O'Hern, S. C.; Jang, D.; Bose, S.; Idrobo, J. C.; Song, Y.; Laoui, T.; Kong, J.; Karnik, R. Nanofiltration across Defect-Sealed Nanoporous Monolayer Graphene. *Nano Lett.* **2015**, *15*, 3254–3260.
- (16) Wang, L.; Boutilier, M. S. H.; Kidambi, P. R.; Jang, D.; Hadjiconstantinou, N. G.; Karnik, R. Fundamental Transport Mechanisms, Fabrication and Potential Applications of Nanoporous Atomically Thin Membranes. *Nat. Nanotechnol.* **2017**, *12*, 509–522.
- (17) Buchheim, J.; Wyss, R. M.; Kim, C.-M.; Deng, M.; Park, H. G. Architecture and Transport Properties of Membranes out of Graphene. *Membr. J.* **2016**, *26*, 239–252.
- (18) Zheng, S.; Tu, Q.; Urban, J. J.; Li, S.; Mi, B. Swelling of Graphene Oxide Membranes in Aqueous Solution: Characterization of Interlayer Spacing and Insight into Water Transport Mechanisms. *ACS Nano* **2017**, *11*, 6440–6450.
- (19) Turchanin, A.; Götzhäuser, A. Carbon Nanomembranes. *Adv. Mater.* **2016**, *28*, 6075–6103.
- (20) Angelova, P.; Vieker, H.; Weber, N.-E.; Matei, D.; Reimer, O.; Meier, I.; Kurasch, S.; Biskupek, J.; Lorbach, D.; Wunderlich, K.; Chen, L.; Terfort, A.; Klapper, M.; Müllen, K.; Kaiser, U.; Götzhäuser, A.; Turchanin, A. A Universal Scheme to Convert Aromatic Molecular Monolayers into Functional Carbon Nanomembranes. *ACS Nano* **2013**, *7*, 6489–6497.
- (21) Delamarche, E.; Michel, B.; Gerber, C.; Anselmetti, D.; Guntherodt, H. J.; Wolf, H.; Ringsdorf, H. Real-Space Observation of Nanoscale Molecular Domains in Self-Assembled Monolayers. *Langmuir* **1994**, *10*, 2869–2871.
- (22) Korolkov, V. V.; Allen, S.; Roberts, C. J.; Tandler, S. J. B. High-Temperature Adsorption of P-Terphenylthiol on Au(111) Surfaces. *J. Phys. Chem. C* **2011**, *115*, 14899–14906.
- (23) Bashir, A.; Azzam, W.; Rohwerder, M.; Terfort, A. Polymorphism in Self-Assembled Terphenylthiolate Monolayers on Au(111). *Langmuir* **2013**, *29*, 13449–13456.
- (24) Briggs, D.; Grant, J. T. *Surface Analysis by Auger and X-ray Photoelectron Spectroscopy*; Surface Spectra: Manchester, UK, 2003.
- (25) Turchanin, A.; Käfer, D.; El-Desawy, M.; Wöll, C.; Witte, G.; Götzhäuser, A. Molecular Mechanisms of Electron-Induced Cross-Linking in Aromatic Sams. *Langmuir* **2009**, *25*, 7342–7352.
- (26) Houplin, J.; Dablemont, C.; Sala, L.; Lafosse, A.; Amiaud, L. Electron Processing at 50 eV of Terphenylthiol Self-Assembled Monolayers: Contributions of Primary and Secondary Electrons. *Langmuir* **2015**, *31*, 13528–13534.
- (27) Heister, K.; Zharnikov, M.; Grunze, M.; Johansson, L. S. O.; Ulman, A. Characterization of X-ray Induced Damage in Alkanethiolate Monolayers by High-Resolution Photoelectron Spectroscopy. *Langmuir* **2001**, *17*, 8–11.
- (28) ASTM E96/E96m-16, Standard Test Methods for Water Vapor Transmission of Materials; ASTM International: West Conshohocken, PA, 2016.
- (29) Li, X.; Wang, R.; Wicaksana, F.; Tang, C.; Torres, J.; Fane, A. G. Preparation of High Performance Nanofiltration (NF) Membranes Incorporated with Aquaporin Z. *J. Membr. Sci.* **2014**, *450*, 181–188.
- (30) McCullough, E. A.; Kwon, M.; Shim, H. A Comparison of Standard Methods for Measuring Water Vapour Permeability of Fabrics. *Meas. Sci. Technol.* **2003**, *14*, 1402–1408.
- (31) Bowden, F. P.; Throssell, W. R. Adsorption of Water Vapour on Solid Surfaces. *Nature* **1951**, *167*, 601–602.
- (32) Breck, D. W. *Zeolite Molecular Sieves: Structure, Chemistry, and Use*; John Wiley & Sons, Inc.: New York, 1974.
- (33) García, R.; San Paulo, A. Attractive and Repulsive Tip-Sample Interaction Regimes in Tapping-Mode Atomic Force Microscopy. *Phys. Rev. B: Condens. Matter Mater. Phys.* **1999**, *60*, 4961–4967.
- (34) Walz, T.; Smith, B. L.; Zeidel, M. L.; Engel, A.; Agre, P. Biologically Active Two-Dimensional Crystals of Aquaporin Chip. *J. Biol. Chem.* **1994**, *269*, 1583–1586.
- (35) Borgia, M. J.; Kozono, D.; Calamita, G.; Maloney, P. C.; Agre, P. Functional Reconstitution and Characterization of Aqpz, the E. Coli Water Channel Protein. *J. Mol. Biol.* **1999**, *291*, 1169–1179.
- (36) Sun, C.; Boutilier, M. S. H.; Au, H.; Poesio, P.; Bai, B.; Karnik, R.; Hadjiconstantinou, N. G. Mechanisms of Molecular Permeation through Nanoporous Graphene Membranes. *Langmuir* **2014**, *30*, 675–682.
- (37) Köfinger, J.; Hummer, G.; Dellago, C. Single-File Water in Nanopores. *Phys. Chem. Chem. Phys.* **2011**, *13*, 15403–15417.
- (38) Zhang, X.; Neumann, C.; Angelova, P.; Beyer, A.; Götzhäuser, A. Tailoring the Mechanics of Ultrathin Carbon Nanomembranes by Molecular Design. *Langmuir* **2014**, *30*, 8221–8227.
- (39) Nečas, D.; Klapetek, P. Gwyddion: An Open-Source Software for Spm Data Analysis. *Cent. Eur. J. Phys.* **2012**, *10*, 181–188.
- (40) Greenspan, L. Humidity Fixed Points of Binary Saturated Aqueous Solutions. *J. Res. Natl. Bur. Stand., Sect. A* **1977**, *81A*, 89–89.
- (41) Firpo, G.; Angeli, E.; Repetto, L.; Valbusa, U. Permeability Thickness Dependence of Polydimethylsiloxane (PDMS) Membranes. *J. Membr. Sci.* **2015**, *481*, 1–8.